

Al-Rich AlGaN Channel High Electron Mobility Transistors on Silicon: A Relevant Approach for High Temperature Stability of Electron Mobility

Julien Bassaler,* Jash Mehta, Idriss Abid, Leszek Konczewicz, Sandrine Juillaguet, Sylvie Contreras, Stéphanie Rennesson, Sebastian Tamariz, Maud Nemoz, Fabrice Semond, Julien Pernot, Farid Medjdoub, Yvon Cordier, and Philippe Ferrandis

Ultrawide bandgap (UWBG) semiconductors offer new possibilities to develop power electronics. High voltage operation for the off-state as well as high temperature stability of the devices in on-state are required. More than AlGaN/GaN heterostructures, AlGaN/AlGaN heterostructures are promising candidates to meet these criteria. Furthermore, the possibility to choose the Al molar fraction of AlGaN paves the way to more tunable heterostructures. In this study, the electronic transport properties of AlGaN channel heterostructures grown on silicon substrates with various aluminum contents, focusing on the temperature dependence of the electron mobility, is investigated. Experimental results from Hall effect measurements are confronted with carrier scattering models and deep level transient spectroscopy analysis to quantify limiting effects. These results demonstrated the significant potential of Al-rich AlGaN channel heterostructures grown on silicon substrates for high power and high temperature applications.

HEMTs: metal-insulator-semiconductor (MIS) gate structure to reduce the gate leakage, recessed-gate or p-GaN gate to achieve normally-off operation, field-plates design to reduce the electrical field peaks, new buffer structures to enhance the crystal quality, introduction of deep-level acceptors such as carbon to increase the resistivity of the buffer, and trap analysis to investigate the effect of the voltage, the gate length and the barrier etching.^[2-20]

Despite all these improvements, the applications of AlGaN/GaN HEMTs in the power market are mainly limited to 650 V. Applications beyond kV are dedicated to SiC-based devices, but at a higher cost than Si-based devices. To expect the development of power devices

1. Introduction

The first AlGaN/GaN high electron mobility transistor (HEMT) was reported in 1993 by Khan et al.^[1] Since then, various solutions were proposed to enhance the performances of AlGaN/GaN

with silicon carbide performances at silicon cost, an alternative to GaN channel HEMT needs to be explored. Aluminum nitride offers more interesting perspectives for power applications than gallium nitride thanks to its wider bandgap and higher critical electric field. Therefore, AlGaN/AlGaN HEMTs are promising

J. Bassaler, J. Pernot, P. Ferrandis
Univ. Grenoble Alpes
CNRS
Grenoble INP
Institut Néel
Grenoble 38000, France
E-mail: julien.bassaler@neel.cnrs.fr

J. Mehta, I. Abid, F. Medjdoub
IEMN
CNRS
Université de Lille
Villeneuve d'Ascq 59650, France

L. Konczewicz, S. Juillaguet, S. Contreras
Laboratoire Charles Coulomb
Univ Montpellier
CNRS
UMR 221, Montpellier 34095, France
L. Konczewicz
Institute of High Pressure Physics
Polish Academy of Sciences
Warsaw 01-142, Poland
S. Rennesson
EasyGAN SAS
Rue Bernard Grégoire, Sophia Antipolis, Cedex 06905, France
S. Tamariz, M. Nemoz, F. Semond, Y. Cordier
Université Côte d'Azur
CNRS
CRHEA
rue Bernard Grégoire, Valbonne 06560, France

 The ORCID identification number(s) for the author(s) of this article can be found under <https://doi.org/10.1002/aelm.202400069>

© 2024 The Authors. Advanced Electronic Materials published by Wiley-VCH GmbH. This is an open access article under the terms of the Creative Commons Attribution License, which permits use, distribution and reproduction in any medium, provided the original work is properly cited.

DOI: [10.1002/aelm.202400069](https://doi.org/10.1002/aelm.202400069)

candidates to surpass the performances of existing AlGaN/GaN HEMTs, especially the breakdown electric field.

Such a solution was first reported by Nanjo et al. in 2008, with an $\text{Al}_{0.20}\text{Ga}_{0.80}\text{N}$ channel HEMT.^[21] They have demonstrated an increase of the breakdown electric field by increasing the Al molar fraction in the channel, from 0.11 MV cm^{-1} for a GaN channel, to 0.67 and 1.61 MV cm^{-1} for $\text{Al}_{0.16}\text{Ga}_{0.84}\text{N}$ channel and $\text{Al}_{0.38}\text{Ga}_{0.62}\text{N}$ channel HEMTs, respectively.^[22] Tokuda et al. realized an $\text{Al}_{0.51}\text{Ga}_{0.49}\text{N}$ channel HEMT, with a breakdown electric field $\approx 1.35 \text{ MV cm}^{-1}$.^[23] Nanjo et al. obtained a breakdown voltage of 1700 V with a $10 \mu\text{m}$ gate-drain space on an $\text{Al}_{0.15}\text{Ga}_{0.85}\text{N}$ channel HEMT.^[24] Li et al. reported the first $\text{Al}_{0.18}\text{Ga}_{0.81}\text{N}$ channel metal insulator semiconductor high electron mobility transistor (MIS-HEMT) in 2015, with a breakdown voltage of 1661 V for a $20 \mu\text{m}$ gate-drain space.^[25] A breakdown voltage of 2200 V was obtained on an $\text{Al}_{0.10}\text{Ga}_{0.90}\text{N}$ channel HEMT by using a hybrid ohmic/Schottky drain contact.^[26] Recently, a breakdown voltage above 4 kV was achieved with an $\text{AlN}/\text{Al}_{0.50}\text{Ga}_{0.50}\text{N}$ MIS-HEMT and a $40 \mu\text{m}$ gate-drain space.^[27]

Regarding temperature operation in on-state, Hatano et al. obtained a drain current reduction of $\approx 65\%$ in the temperature range of $25\text{--}300^\circ\text{C}$ for a GaN channel HEMT, whereas the reduction was half this value for the $\text{Al}_{0.24}\text{Ga}_{0.76}\text{N}$ channel HEMT.^[28] In the same temperature range, Tokuda et al. reported a reduction of less than 20% for the $\text{Al}_{0.51}\text{Ga}_{0.49}\text{N}$ channel HEMT, compared to 80% for the GaN channel HEMT.^[23] Li et al. reported a drain current decrease of 20% in the temperature range of $25\text{--}275^\circ\text{C}$ on the $\text{Al}_{0.18}\text{Ga}_{0.82}\text{N}$ channel MIS-HEMT.^[25]

The performances of (Al,Ga)N channel HEMTs strongly depend on the choice of the substrate.^[29] Most of the AlGaN channel heterostructures reported in the literature were grown on a sapphire substrate.^[21,22,24\text{--}27,30\text{--}44] The comparison between heterostructures grown on sapphire and AlN substrates has shown that the better crystal quality obtained on AlN enhances the device performances.^[32] The higher thermal conductivity, the higher breakdown electric field and the lower lattice mismatch that offers AlN compared to sapphire allows it to obtain excellent performances.^[23,28,32,45\text{--}47] However, its high cost combined with a maximum available wafer size of $2\text{--}4$ inches limit its industrial development. Therefore, structures grown on silicon substrates appear more suitable to ensure a low fabrication cost and an improved competitiveness on the power electronics market.

The AlGaN channel has already proven its efficiency on the breakdown voltage increase and the operation stability at high temperature.^[23,28] The electron mobility is also a key parameter which needs to be carefully investigated since it depends directly on the Al molar fraction in the AlGaN channel. Higher electron mobility allows faster switching speed and higher on-state current density. With an $\text{Al}_{0.06}\text{Ga}_{0.94}\text{N}$ channel HEMT, Raman et al. determined an electron mobility of $590 \text{ cm}^2 \text{ V}^{-1} \text{ s}^{-1}$.^[48] Nanjo et al. obtained values of 460 and $545 \text{ cm}^2 \text{ V}^{-1} \text{ s}^{-1}$ for an $\text{Al}_{0.15}\text{Ga}_{0.85}\text{N}$ channel HEMT grown on sapphire and SiC respectively.^[30] Electron mobilities of 175 and $284 \text{ cm}^2 \text{ V}^{-1} \text{ s}^{-1}$ were obtained for $\text{Al}_{0.60}\text{Ga}_{0.40}\text{N}$ channel and $\text{Al}_{0.65}\text{Ga}_{0.35}\text{N}$ channel HEMTs, respectively.^[36,44] For an $\text{Al}_{0.70}\text{Ga}_{0.30}\text{N}$ channel HEMT, Klein et al. determined an electron mobility of $240 \text{ cm}^2 \text{ V}^{-1} \text{ s}^{-1}$, where Baca et al. reached $390 \text{ cm}^2 \text{ V}^{-1} \text{ s}^{-1}$ for the same composition, but with a 2DEG density half as high.^[38,49] This work aims to study the impact of the aluminum molar fraction increase in the AlGaN

channel heterostructures grown on a Si (111) substrate on the electron mobility and its thermal stability.

2. Devices Fabrication

Three AlGaN/AlGaN heterostructures were grown by ammonia molecular beam epitaxy (NH_3 -MBE) on a 3 inches diameter Si (111) substrate.^[50] The structures, as shown in Figure 1(a), are composed of a 200 nm AlN nucleation layer, a 450 nm AlGaN channel, a 1 nm thin AlN spacer, a 10 nm AlGaN barrier and a 1 nm GaN cap layer. The Al molar fraction in the channel (x_C) was fixed to 10% , 30% and 60% , and the Al molar fraction in the barrier (x_B) was fixed to 60% , 70% and 90% respectively. It results from calculations (see Experimental methods section for the simulation details) a 2D electron gas (2DEG) density of 1.71×10^{13} , 1.39×10^{13} , and $0.65 \times 10^{13} \text{ cm}^{-2}$ at room temperature for 10% , 30% and 60% of Al in the channel, respectively. The corresponding conduction band minimum E_C of the three samples obtained by simulations is shown in Figure 1(b).

Ohmic contacts were fabricated by partially etching the AlGaN barrier followed by e-beam evaporation of $12/200/40/100 \text{ nm}$ Ti/Al/Ni/Au metal stack and a rapid thermal annealing set at $850\text{--}875^\circ\text{C}$ during 30 s . Mesa isolation of 220 nm depth was achieved by inductively coupled plasma etching technique. Plasma enhanced chemical vapor deposition of 30 nm thick SiN was used for the passivation of the surface.

3. Theoretical Transport Properties of AlGaN Channel Heterostructures

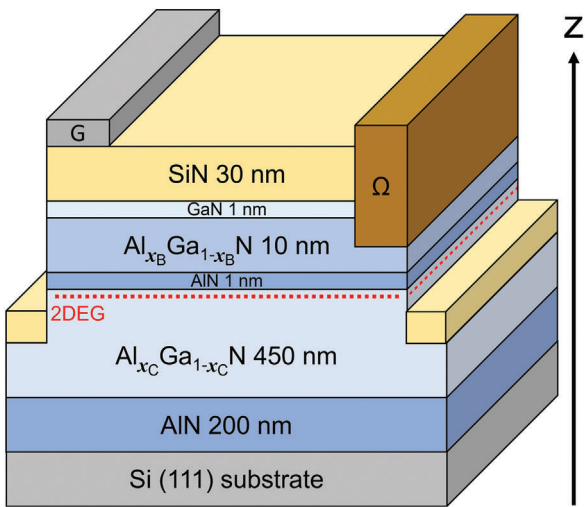
The electron mobility can be expressed as $\mu_n = (q/m_n^*) \times \langle \tau(E) \rangle$, where μ_n is the electron mobility, q is the electron elementary charge, m_n^* is the electron effective mass, and $\langle \tau(E) \rangle$ is the energy-dependent mean electron relaxation time. In a degenerated case, as for a 2DEG, the electron occupation is given by the Fermi-Dirac statistics and its derivative can be approximated to unity close to the Fermi level and zero otherwise.^[51] Thus, the mean electron relaxation time can be considered as energy-independent. The electron mobility μ_n can be linked to the different scattering mechanisms by the Matthiessen's rule as:

$$\frac{1}{\mu_n} \approx \sum_i \frac{1}{\mu_i} \approx \frac{m_n^*}{q} \sum_i \frac{1}{\tau_i} \quad (1)$$

where μ_i is the mobility of the considered scattering mechanism, and τ_i is the corresponding momentum relaxation time.

Two main effects are responsible for the electron mobility limitation. Independently of the temperature carrier scattering results from crystal defects and alloy disorder, which are mainly growth-dependent. When the temperature increases, the electron-phonon interactions become stronger and limit the electron transport. Here, we have neglected the carrier-carrier scattering effect. Scattering models for 2D conduction have been widely developed through the years and many papers have proven their reliability for AlGaN/GaN heterostructures.^[52\text{--}57] In this work, interface roughness (IFR), threading dislocations (DIS) and alloy disorder (ADO) are considered as structure related effects.

(a)



(b)

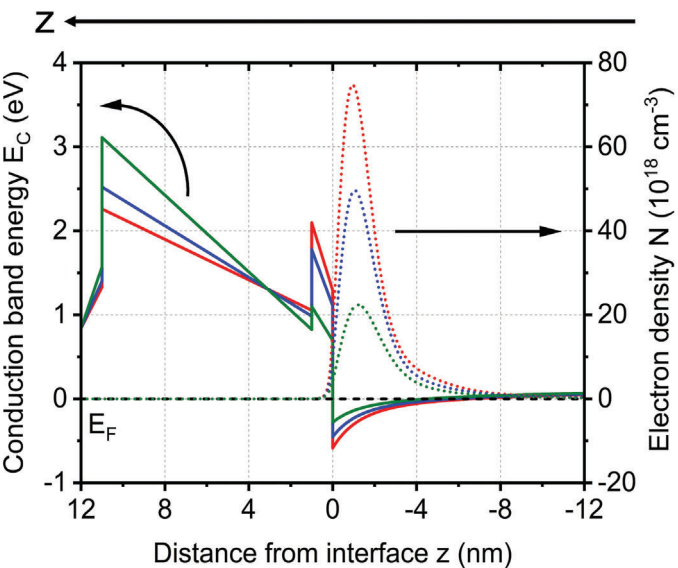


Figure 1. a) 3D schematic cross-section of the studied AlGaN channel heterostructures after the mesa isolation, contact deposition and surface passivation. b) Minimum of the conduction band E_C (solid lines) and volume electron density N (dashed lines) of the GaN/AlGaN/AlN/AlGaN stack for an AlGaN channel with an Al molar fraction of 10% (red), 30% (blue), and 60% (green).

Electron-phonon interactions are described by acoustic phonons (AP) effects, regrouping deformation-potential (DP) and piezoelectric (PE) contributions, and by polar optical phonons (POP) effect. The analytical expressions of the models, as well as material parameters used in calculations, are presented in Supporting Information.

The calculated electron mobility μ_n as a function of the Al molar fraction in the channel x_C is presented in **Figure 2(a–c)** at 10, 300 and 600 K, respectively. The calculations have been performed assuming a constant 2DEG density n_{2D} of 10^{13} cm^{-2} and using parameter values in Tables S1 and S2 (Supporting Information). To maintain a constant 2DEG density for each value of x_C , an appropriate value of x_B should be considered. The assumption of a constant n_{2D} of 10^{13} cm^{-2} is only possible for a large enough conduction band offset between the channel and the barrier. Bacă et al. have determined that a 2DEG density of 10^{13} cm^{-2} is possible to obtain for an Al fraction in the channel x_C up to 85%, which ensure a sufficient conduction band offset.^[58] Therefore, calculated data are only presented for an Al fraction x_C from 0% to 85%, and for each value of x_C corresponds a value of x_B , which does not get involved into the calculations, and therefore has not been specified.

Figure 2(a), shows that at 10 K the alloy disorder represents the main limitation for the mobility on the whole composition range, so that the total mobility is completely overlapped with the ADO mobility. In **Figure 2(b)**, at 300 K, the phonons are more impactfull, but the mobility is still mainly limited by the alloy disorder. In **Figure 2(c)**, at 600 K, the polar optical phonons have a strong impact on the total mobility, but still are less impactfull than the alloy disorder for an Al composition range of 0.20–0.85. The dislocation and interface roughness scattering do not play an important role in the electron mobility reduction compared to the alloy disorder. **Figure 2(d)**

summarizes the total electron mobility for the three temperatures. The electron mobility appears to be less reduced when increasing the temperature for Al molar fractions ≈ 0.55 .

For a GaN channel, the ADO effect is only considered in the AlGaN barrier and is often negligible compared to other structure-related scattering effects such as dislocations and interface roughness.^[59] Consequently, in **Figure 3(a)**, at low temperature and for a GaN channel ($x_C = 0$), without considering IFR and DIS effects, the mobility is limited by AP. If we now consider IFR and DIS effects, we observe a reduced and less temperature-dependent mobility due to the temperature independence of IFR and DIS scattering modes. By adding the ADO effect for AlGaN, the mobility is further reduced but also less temperature dependent. At high temperature, POP effect is responsible for the mobility drop. In this region, the total mobility can be approximated by $\mu_n \propto T^{-\alpha}$, where α is a dimensionless temperature coefficient. In **Figure 3(b)**, where the temperature coefficient α is presented versus the Al molar fraction in the channel x_C , for $x_C = 0$, a temperature coefficient close to 2 is observed. This temperature dependence about T^{-2} is directly linked to the theoretical model of POP effect (see Supporting Information). When increasing the Al fraction, the temperature coefficient reaches a minimum close to 0.5 for $x_C = 0.55$. Actually, the ADO scattering mechanism being temperature independent ($\mu_{ADO} \propto T^0$), the temperature coefficient α will decrease as the intensity of the alloy disorder effect increases compared to POP effect. In fact, it has also been suggested that the weaker temperature dependence of the AlGaN channel HEMTs compared to GaN channel HEMTs is partly due to the temperature independence of the ADO and IFR limiting mechanisms.^[45,60]

Electron mobility significantly influences the efficiency of electronic devices. Moreover, for high power switching applications,

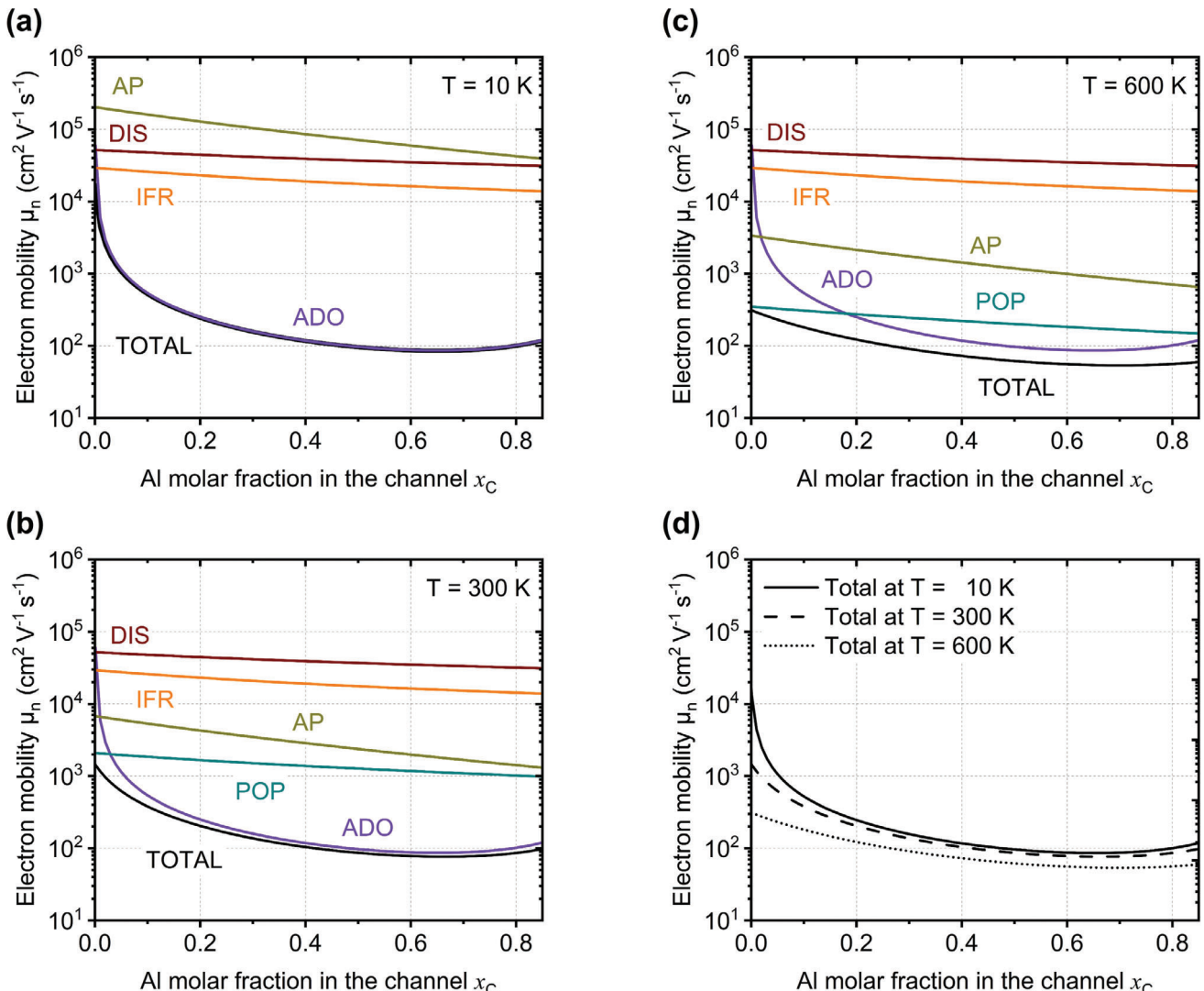


Figure 2. Calculated low-field electron mobility μ_n in AlGaN channel heterostructures as a function of the Al molar fraction in the channel x_C , assuming a constant 2DEG density n_{2D} of 10^{13} cm^{-2} , at a) 10 K, b) 300 K, and c) 600 K. d) Summary of the total calculated electron mobility μ_n as a function of the Al molar fraction in the channel x_C at 10, 300, and 600 K. Parameter values from Tables S1 and S2 (Supporting Information) were used for calculations. AP: acoustic phonons – POP: polar optical phonons – IFR: interface roughness – DIS: dislocations – ADO: alloy disorder. The lower the mobility value associated with a scattering mechanism, the stronger the intensity of that mechanism.

a high breakdown voltage V_{br} and a low specific on-resistance $R_{on,sp}$ are also required. The Baliga's figure of merit (BFOM) has been formulated to compare the potential of semiconductors for power-switching, and is expressed as $BFOM = \epsilon_{sc}\mu_n E_{cr}^3$, where ϵ_{sc} is the semiconductor permittivity, and E_{cr} is the critical electric field. However, the conventional BFOM only applies for vertical devices. For HEMTs, the lateral figure of merit (LFOM) is used, given by:^[61,62]

$$LFOM = \frac{V_{br}^2}{R_{on,sp}} = q n_{2D} \mu_n E_{cr}^2 \quad (2)$$

Hudgins et al. have determined that the critical electric field for a direct bandgap semiconductor can be approximated by the equation $E_{cr} = 1.73 \times 10^5 (E_g)^{2.5}$.^[63] To determine the LFOM of

AlGaN channel HEMT, we used this relation. The bandgap E_g has been calculated using a quadratic interpolation from the bandgap of the binary materials AlN and GaN, as described in the Supporting Information. The temperature dependence of the critical electric field has been neglected.

From calculations of temperature dependency of LFOM presented in Figure 4(a), at 300 K, an AlGaN channel HEMT with 85% of Al has a similar LFOM than a GaN channel HEMT. When increasing the temperature, the same LFOM is obtained for a lower Al fraction. Our findings correspond to the LFOM from the theoretical investigation conducted by Baja et al., wherein the influence of alloy disorder and polar optical phonon scattering mechanisms alone were considered.^[61] The Figure 4(b) represents the Al fraction required to obtain the same LFOM for a GaN channel than for an AlGaN channel as

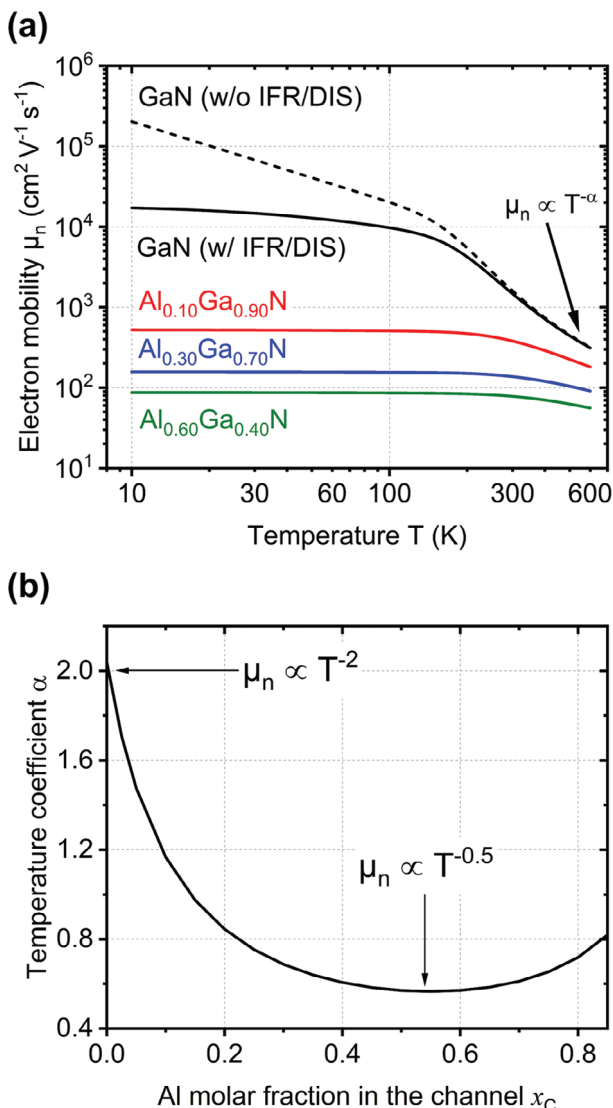


Figure 3. a) Calculated low-field electron mobility μ_n in AlGaN channel heterostructures as a function of temperature for an Al molar fraction in the channel x_C of 0% without IFR and DIS effects (dashed line), 0% (solid line), 10% (red), 30% (blue) and 60% (green). b) Calculated temperature coefficient as a function of the Al molar fraction in the channel x_C , using parameter values of Tables S1 and S2 (Supporting Information).

a function of temperature. The equivalent Al fraction to obtain $\text{LFOM}(\text{GaN}) = \text{LFOM}(\text{AlGaN})$ decreases linearly with temperature. Actually, at 600 K, the LFOM of AlGaN channel HEMTs with 56% and 80% of Al is expected to be respectively the same and twice that of a GaN channel HEMT, assuming an identical n_{2D} of 10^{13} cm⁻².

4. Electron Transport Analysis

4.1. Experimental Electron Transport Properties

The measured 2DEG resistivity ρ is reported in Figure 5(a) and its values, extracted at 10, 300 and 600 K, for the heterostructures with 10%, 30% and 60% of Al in the channel, are reported

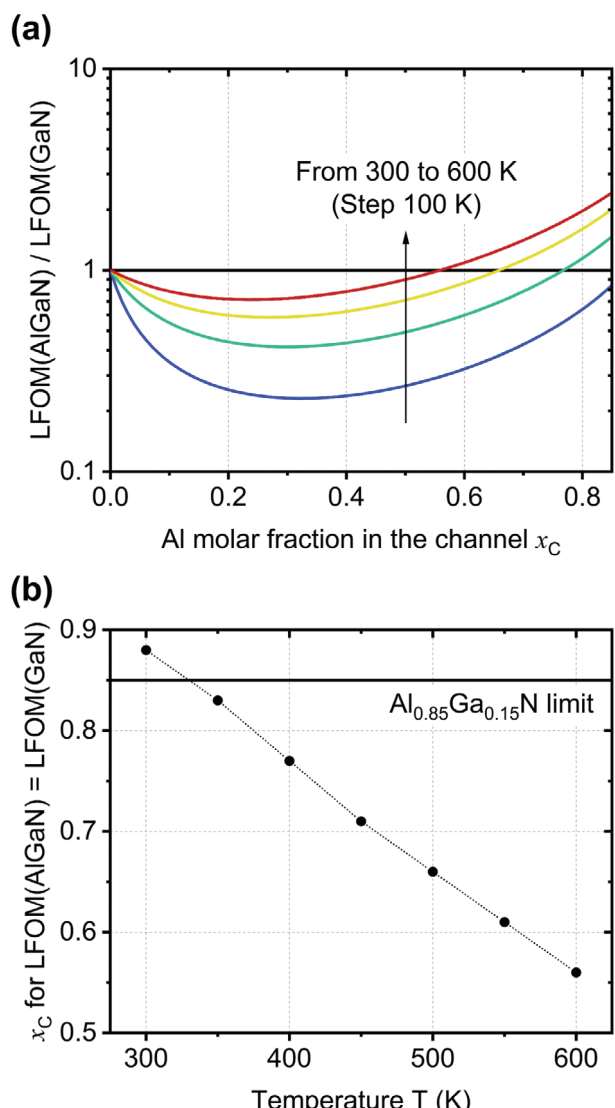


Figure 4. a) Calculated lateral Baliga's figure of merit LFOM as a function of the Al molar fraction in the channel x_C for temperatures from 300 to 600 K. b) Al molar fraction in the channel x_C to obtain the same LFOM between GaN channel and AlGaN channel HEMTs as a function of temperature. Higher is LFOM, lower are the conduction losses.

in Table 1. Three different behaviors can be distinguished in Figure 5(a). From 10 to 125 K, the 2DEG resistivity slowly decreases. From 125 to 400 K, the 2DEG resistivity increases, which is expected for a 2DEG conduction mode. From 400 to 600 K, a drop of resistivity is observed. A dispersion of resistivity values ≈ 300 K is noteworthy for the structure with 60% of Al in the channel, which can be attributed to the high contact resistance, due to the elevated Al content, causing disturbances in the measurements.

The evolution of the Hall density n_H is presented in Figure 5(b) and the extracted values are also summarized in Table 1. At low temperature ($T < 300$ K), for heterostructures with 10% and 30% of Al in the channel, the Hall density is constant, matching well with simulation results. The Hall density for heterostructure with

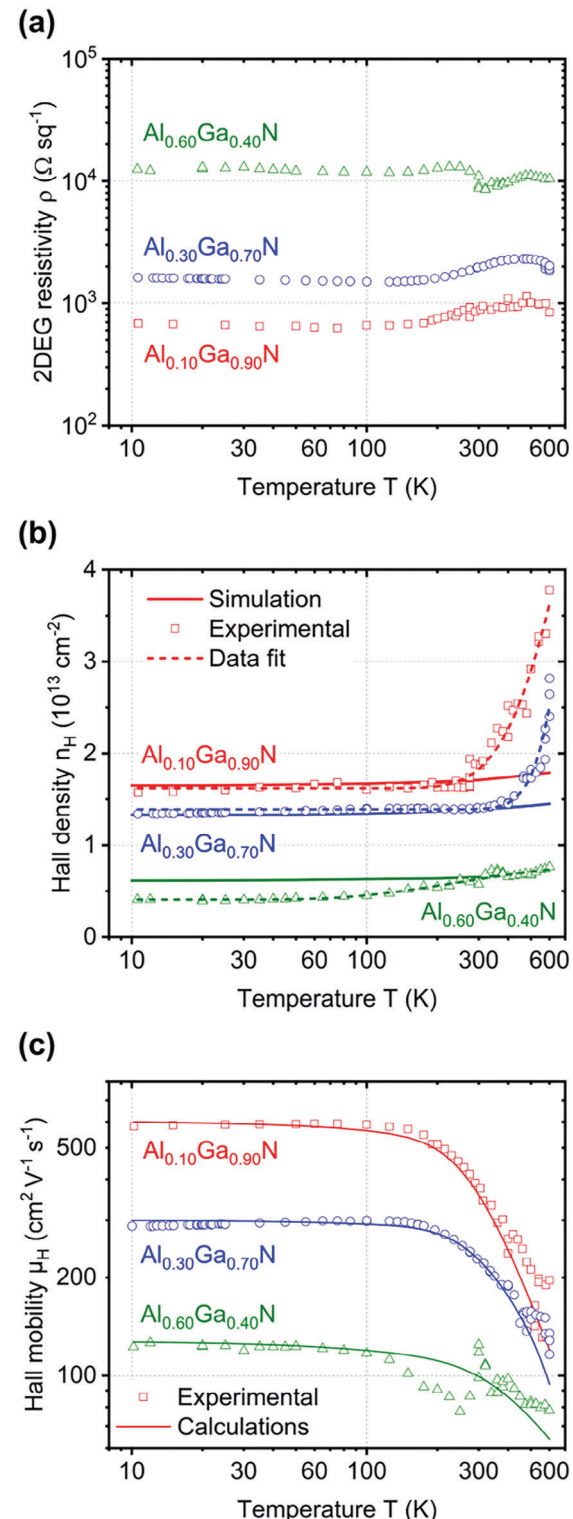


Figure 5. Hall effect results as a function of temperature for heterostructures with 10% (red), 30% (blue) and 60% (green) of Al in the channel. a) 2DEG resistivity ρ . b) Hall density n_H – experimental data (symbols), simulation (solid lines), and exponential data fit (dashed lines) using Equation (3). c) Hall electron mobility μ_H (symbols) and calculated low-field electron mobility μ_n (solid lines) using the parameters of Table S3 (Supporting Information).

60% of Al in the channel is lower than expected from simulations. At 10 K, the Hall density of the heterostructure with 60% of Al in the channel is half of the calculated 2DEG density. This difference reduces when increasing the temperature up to ≈ 300 K, then the calculated and the experimental densities are similar up to 600 K. We suspect that this effect is related to a detrapping effect occurs in this heterostructure from 10 to 300 K, and a trap analysis will be conducted below. At higher temperature ($T > 300$ K), an important increase of the Hall density is observed for heterostructures with 10% and 30% of Al in the channel, which does not correspond to our simulations, where the 2DEG density increase is $\approx +10\%$ on the range 10–600 K. The Hall density increase seems to have a direct link with the resistivity decrease observed in Figure 5(a). The heterostructure with 60% of Al in the channel only presents a slight increase of the Hall density, still in agreement with simulation results (Figure 5(b)). The experimental data have then been fitted with the expression:

$$n_H(T) = n_0 + n_1 \exp\left(\frac{-E_a}{k_B T}\right) \quad (3)$$

where n_0 represents the Hall density at low temperature, i.e., the closest value to the true 2DEG density, n_1 is a coefficient related to the intensity of effect responsible for the electron density increase, and E_a is the thermal activation energy of the process. The extracted values for the heterostructures with 10%, 30% and 60% of Al in the channel are summarized in Table 2. n_0 values are very close to the Hall densities obtained at 10 K (Table 1). Activation energies of 117, 228, and 20 meV have been determined for the heterostructure with 10%, 30%, and 60% of Al in the channel, respectively. Similar 2DEG density behaviors at high temperature have already been obtained in AlGaN/GaN heterostructures. In the study conducted by Consejo et al., the enhancement of the Al fraction in the barrier corresponds to an apparition at a higher temperature of the 2DEG density increase.^[64] This is consistent with our observations from the Figure 5(b), where the Hall density increase appears at higher temperatures as the Al fraction in the AlGaN barrier is increased. The origin of the significant increase in the Hall density has not yet been identified, and further analysis is required.

The corresponding Hall mobility μ_H as a function of temperature is shown in Figure 5(c) and the values at 10, 300 and 600 K are reported in Table 1. The mobility evolution can be separated in two parts: i) a constant mobility from 10 to 125 K, related to the low variation of the 2DEG resistivity ρ and the constant Hall

Table 1. Extracted values of 2DEG resistivity ρ , Hall density n_H , and Hall mobility μ_H , at a temperature of 10, 300 and 600 K, for heterostructures with 10%, 30%, and 60% of Al in the channel.

Al molar fraction in the channel x_C	$\rho (10^3 \Omega \text{ s q}^{-1})$			$n_H (10^{13} \text{ cm}^{-2})$			$\mu_H (\text{cm}^2 \text{ V}^{-1} \text{ s}^{-1})$		
	10 K	300 K	600 K	10 K	300 K	600 K	10 K	300 K	600 K
10%	0.7	0.9	0.8	1.60	1.88	3.78	582	390	196
30%	1.6	1.9	1.9	1.35	1.41	2.82	287	228	116
60%	12.5	11.1	10.7	0.41	0.57	0.71	123	99	82

Table 2. Extracted parameters n_0 , n_1 , and E_a , from the exponential fits of the Hall densities using Equation (3), as a function of temperature, for heterostructures with 10%, 30%, and 60% of Al in the channel.

Al molar fraction in the channel x_C	n_0 (cm^{-2})	n_1 (cm^{-2})	E_a (meV)
10%	$(1.62 \pm 0.03) \times 10^{13}$	$(1.93 \pm 0.38) \times 10^{14}$	117 ± 9
30%	$(1.39 \pm 0.01) \times 10^{13}$	$(2.96 \pm 1.07) \times 10^{15}$	228 ± 18
60%	$(4.06 \pm 0.09) \times 10^{12}$	$(4.85 \pm 0.32) \times 10^{12}$	20 ± 2

density n_H in this temperature range, and ii) a decreasing mobility from 125 to 600 K. Between 125 and 400 K, the reduction of μ_H is related to the increase of the 2DEG resistivity ρ , and beyond 400 K, by the increase of the Hall density n_H . It is worth noting that the Hall mobility of the heterostructure with 60% of Al in the channel presents irregularities between 100 and 300 K, which deviate from the expected behavior, and is attributed to the high contact resistance, as mentioned earlier. Furthermore, a good agreement is observed between experimental and calculated electron mobility, and further details will be provided below. As can be observed in Figure 5(c), the electron mobility is proportionally less degraded when increasing the temperature for Al-rich heterostructures, which is consistent with theoretical results in Figure 3(b). From values extracted in Table 1, the electron mobility degradation between 300 and 600 K is -50%, -49%, and -17% for heterostructures with 10%, 30%, and 60% of Al in the channel.

Deep level transient spectroscopy (DLTS) has been performed on a circular device to investigate the presence of electrically active traps in the heterostructure with 60% of Al in the channel. Current-voltage $J_G(V_G)$ and capacitance-voltage $C(V_G)$ characteristics of the circular device at 77 and 300 K are presented in Figure 6(a). From the capacitance-voltage characteristic at 300 K, we observe a complete depletion of the 2DEG at $V_G = -6.0$ V, where the capacitance reaches a constant value of 17 nF cm^{-2} . Hysteresis can be observed in both the $J_G(V_G)$ and the $C(V_G)$ characteristics at 77 K, with a reduced effect at 300 K, attributed to a detrapping effect. The Figure 6(b) reports the DLTS spectra obtained over the temperature range 77–325 K, with a reverse bias $V_R = -5.0$ V, a pulse voltage $V_p = -0.5$ V, a filling pulse time $t_p = 1$ s, a delay $t_0 = 874 \mu\text{s}$, and a period width $T_W = 10$ ms. A large signal can be observed on the entire temperature range, with a maximum signal amplitude at 255 K, and the presence of a shoulder at 170 K, indicating at least two trap levels, named E_{170} and E_{255} . The identification of E_{170} and E_{255} will not be further discussed in this work, and require deeper investigations. Nevertheless, the presence of traps E_{170} and E_{255} agrees with the hypothesis of a detrapping effect responsible for the difference between experimental and calculated carrier densities at low temperature in the heterostructure with 60% of Al in the channel (Figure 5(b)). It has been demonstrated that the presence of deep traps in semiconductors can significantly increase their resistivity.^[65] As the temperature increases, the detrapping of charge carriers leads to a lower resistivity at high temperature compared to lower temperatures.

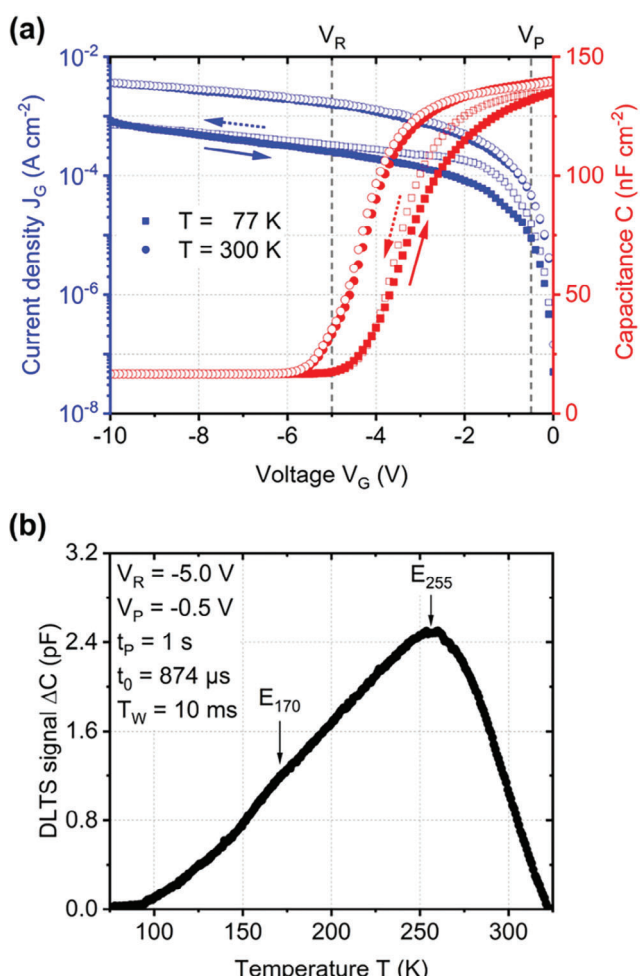


Figure 6. Trap detection analysis of the AlGaN channel heterostructure with 60% of Al in the channel. a) Current density J_G (blue) and surface capacitance C (red) as a function of the gate voltage V_G recorded from -10 to 0 V (closed symbols) and from 0 to -10 V (open symbols) at 77 K (squares) and at 300 K (circles). b) Capacitance DLTS signal ΔC acquired in the temperature range 77–325 K with a reverse bias $V_R = -5.0$ V, a pulse voltage $V_p = -0.5$ V, a filling pulse time $t_p = 1$ s, a delay $t_0 = 874 \mu\text{s}$, and a period width $T_W = 10$ ms. Two traps E_{170} and E_{255} are dominant on the spectra.

This behavior corresponds to our observations on the 2DEG resistivity in Figure 5(a) for the AlGaN channel heterostructure with 60% of Al in the channel. It is important to note that DLTS measurements carried out between 77 K and 325 K on heterostructures with 10% and 30% of Al in the channel did not reveal the existence of deep traps exhibiting amplitudes as significant as those observed in the heterostructure with 60% of Al in the channel. This observation aligns with the match observed at low temperature between the 2DEG density in both experimental measurements and simulated data. Actually, the more the Al fraction is in the channel, the deeper the traps are expected to be in the bandgap, as for instance with silicon or oxygen impurities in AlGaN.^[66,67] This could explain that only the heterostructure with 60% of Al in the channel presents this behavior.

4.2. Confrontation of Experimental and Calculated Electron Mobility

Experimental Hall mobility is compared to the calculated electron mobility of heterostructures with 10%, 30% and 60% of Al in **Figure 7(a–c)**, respectively. In the calculations, we applied the exponential fit described by Equation (3) for the Hall density, whose coefficients are given in Table 2 for each heterostructure. IFR and DIS scattering effects have been maximized, and the ADO scattering effect has been adjusted to the experimental data by taking the alloy potential as a fitting parameter. More details about the structure related scattering mechanisms can be found in Supporting Information. The parameter values used for calculation are summarized in Table S3 (Supporting Information). A good agreement is observed in the whole temperature range. ADO model has been fitted by using an alloy disorder scattering potential of 1.1, 1.2 and 1.7 eV for 10%, 30% and 60% of Al, respectively. The alloy disorder appears to be the main limitation of the electron mobility for the three samples. For 10% of Al in the channel, the interface roughness is however as impactful as the alloy disorder. Actually, the high interface roughness combined with the high carrier density results in a more important interface roughness effect on the electron mobility. With the increase of the Hall density as a function of temperature for the heterostructure with 60% of Al in the channel, the IFR and DIS scattering effects are not constant in the temperature range, but still are less impactful than the ADO scattering effect. At high temperatures, as the Al fraction in the channel increases, the impact of polar optical phonons becomes less significant compared to alloy disorder, even at 600 K (Figure 7(c)). This implies a weaker temperature degradation of the electron mobility obtained when increasing the Al fraction in the channel ($\approx -50\%$ for 10% and 30% of Al, against -17% for 60% of Al).

4.3. Comparison with State-of-the-Art AlGaN Channel Heterostructures

Electron mobility μ_n values at room temperature are summarized as a function of the Al molar fraction in the channel x_C in **Figure 8(a)**, and as a function of the 2DEG density n_{2D} in **Figure 8(b)**. Electron mobility values of AlGaN channel heterostructures on SiC or sapphire substrates from the literature are shown for comparison.^[24,27,31,35,36,38,44,47–49,58,68] The experimental electron mobility is consistent with the expected evolution by adding Al in the channel, namely a decrease of μ_n .

To compare the transport properties of the studied AlGaN channel heterostructures with the literature, the Figure 8(c) indicates the corresponding 2DEG resistivity ρ as a function of the Al molar fraction in the channel x_C . The heterostructure with 10% of Al in the channel exhibits a higher resistivity ($0.9 \text{ k}\Omega \text{ sq}^{-1}$) than the one realized by Singhal et al. on a SiC substrate, with the same Al composition in the channel ($0.7 \text{ k}\Omega \text{ sq}^{-1}$).^[47] On the opposite, the heterostructure with 30% of Al presents a lower resistivity ($1.9 \text{ k}\Omega \text{ sq}^{-1}$) than the structure with the same Al fraction of Klein et al. ($2.9 \text{ k}\Omega \text{ sq}^{-1}$) on a sapphire substrate.^[68] Our heterostructure with 60% of Al in the channel suffers from higher resistivity ($11.1 \text{ k}\Omega \text{ sq}^{-1}$) than reported in the literature for the same Al fraction, as for example from Xue et al. ($4.2 \text{ k}\Omega \text{ sq}^{-1}$)^[44] or from Klein

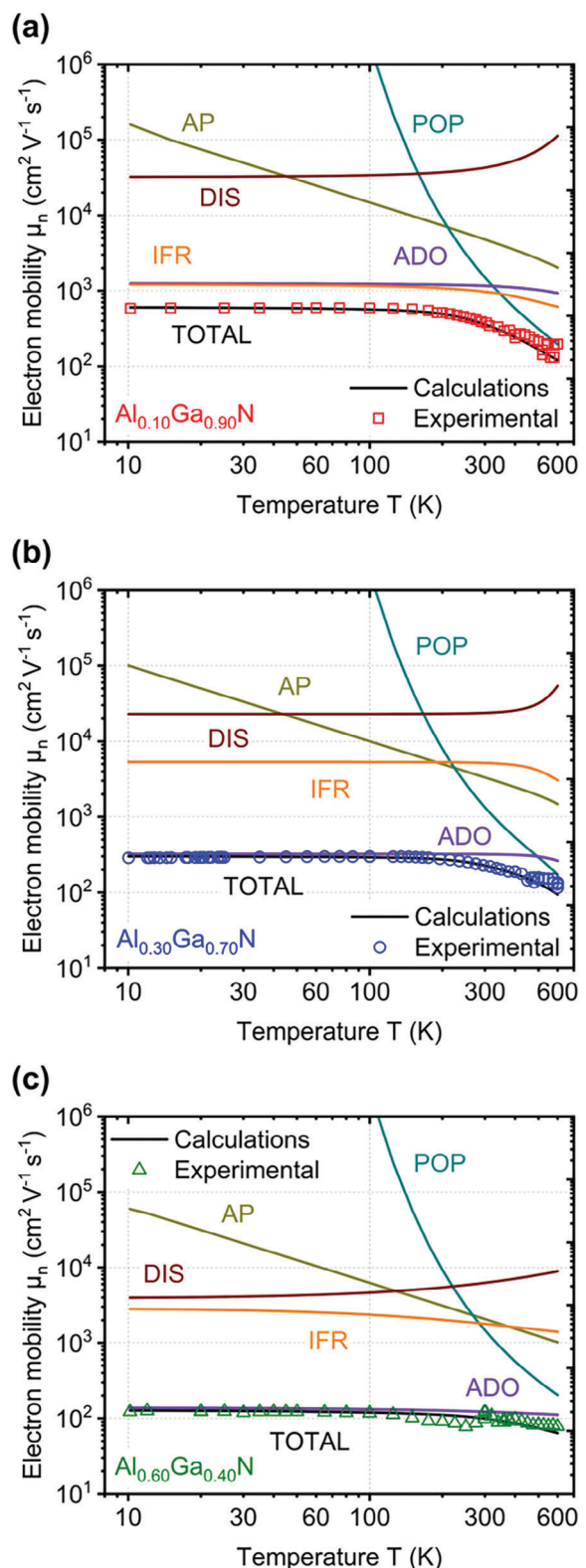


Figure 7. Experimental (symbols) and calculated (lines) electron mobility as a function of temperature, using parameters in Table S3 (Supporting Information) for calculations, for a) 10%, b) 30% and c) 60% of Al molar fraction in the channel. AP: acoustic phonons – POP: polar optical phonons – IFR: interface roughness – DIS: dislocations – ADO: alloy disorder.

[24] [27] [31] [35] [36] [38] [44] [47] [48] [49] [58] [68]

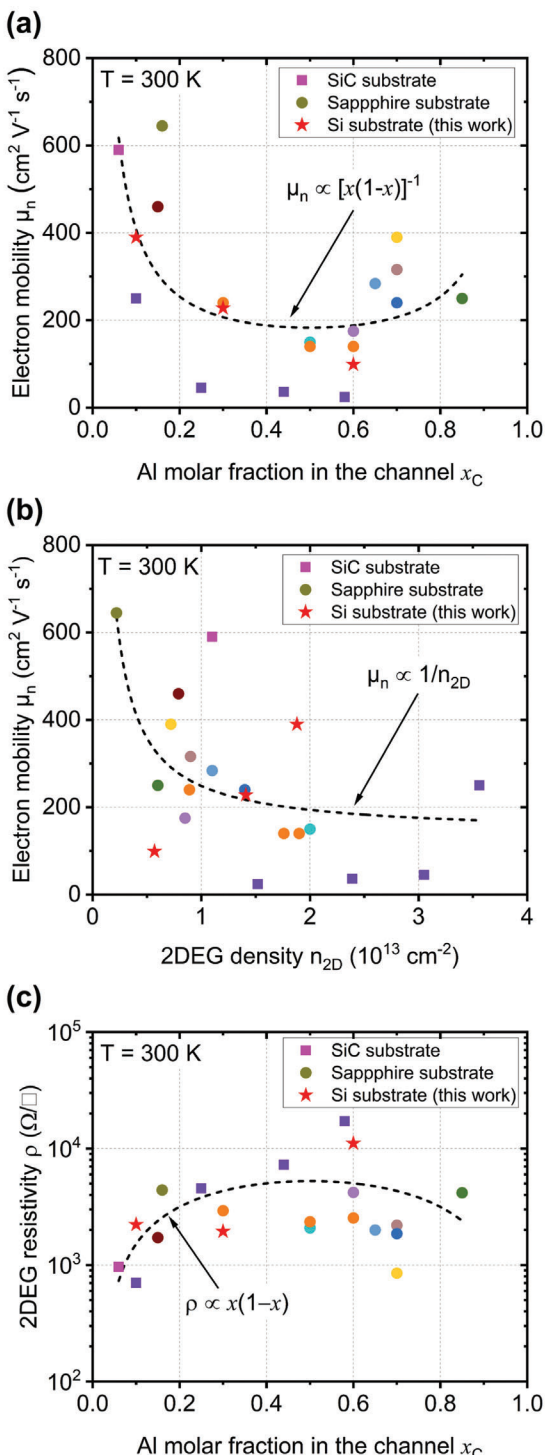


Figure 8. Experimental values of electron mobility μ_n at room temperature, as a function of a) Al molar fraction in the channel x_C and b) 2DEG density n_{2D} . c) 2DEG resistivity ρ as a function of Al molar fraction in the channel x_C . Data are taken from this work on a Si substrate (red stars), and from previous works on SiC or sapphire substrates^[24,27,31,35,36,38,44,47–49,58,68] (squares: SiC substrate – circles: sapphire substrate). Dashed lines serve as a visual guide.

et al. ($2.5 \text{ k}\Omega \text{ sq}^{-1}$).^[68] The resolution of trapping effects and high contact resistance is expected to enhance the transport properties of this kind of heterostructure in the future. Nonetheless, the AlGaN channel heterostructures realized on a silicon substrate exhibit similar electron mobility than for structures on SiC or sapphire substrates.

5. Conclusions

The temperature dependence of the theoretical and experimental electron mobility has been studied on AlGaN channel heterostructures with 10%, 30% and 60% of Al in the channel, and with appropriate Al compositions in the barrier allowing to obtain the same 2DEG density $n_{2D} = 10^{13} \text{ cm}^{-2}$. From calculations, an AlGaN channel heterostructure with an Al molar fraction close to 0.55 is expected to be as efficient as a GaN channel heterostructure at 600 K, with a weaker degradation of the electron mobility. From Hall effect measurements, Hall densities n_H of 1.88×10^{13} , 1.41×10^{13} and $0.57 \times 10^{13} \text{ cm}^{-2}$, and Hall mobilities μ_H of 390, 224 and $99 \text{ cm}^2 \text{ V}^{-1} \text{ s}^{-1}$ have been extracted at room temperature for channels with 10%, 30% and 60% of Al, respectively. The Al enrichment of the channel leads to an increase of the resistivity ρ , related to the electron mobility reduction. At low temperature ($T < 300 \text{ K}$), the lower Hall density for the structure with 60% of Al has been attributed to the presence of at least two deep traps detected by DLTS over the temperature range 77–325 K. The three heterostructures exhibit an electron mobility drop at high temperature of –50%, –49%, and –17%, from 300 to 600 K, and for an Al fraction of 10%, 30%, and 60%, respectively, indicating the lower temperature dependence of the electron mobility in Al-rich channels. At high temperature ($T > 400 \text{ K}$), a decrease of the 2DEG resistivity associated with an increase of the Hall density has been observed in structures with 10% and 30% of Al, but not for 60% of Al. Structural analysis and simulations have been used to adjust electron scattering models, which are in good agreement with the experimental data on the studied temperature range (10–600 K). The electron mobility in the AlGaN channel heterostructures is mainly limited by the alloy disorder, whose impact is stronger for Al-rich channels, as demonstrated by the growing fitted values of the alloy scattering potential with the Al content. The interface roughness scattering also appears to be a limitation for the AlGaN channel with 10% of Al. At high temperature, polar optical phonons are responsible for the electron mobility drop, but are less impactful as the Al molar fraction in the channel increases. The studied heterostructures, grown on a silicon substrate, exhibit transport properties comparable to state-of-the-art reported on SiC or sapphire substrates. These results highlight the potential of Al-rich AlGaN channel heterostructures on silicon for high temperature applications. However, by increasing the Al content in the channel and the barrier, the 2DEG density seems to be limited by the presence of deep traps. Moreover, the contact resistance rapidly increases. This represents the actual limitations of these devices, and outmatch these technological steps is the key to expect further developments. The reduction of the trap density in the Al-rich structures could help to enhance the 2DEG density. A buffer engineering is then required to increase the crystal quality in the channel. The regrowth of ohmic contacts is expected to be an efficient solution to reduce the contact resistance.

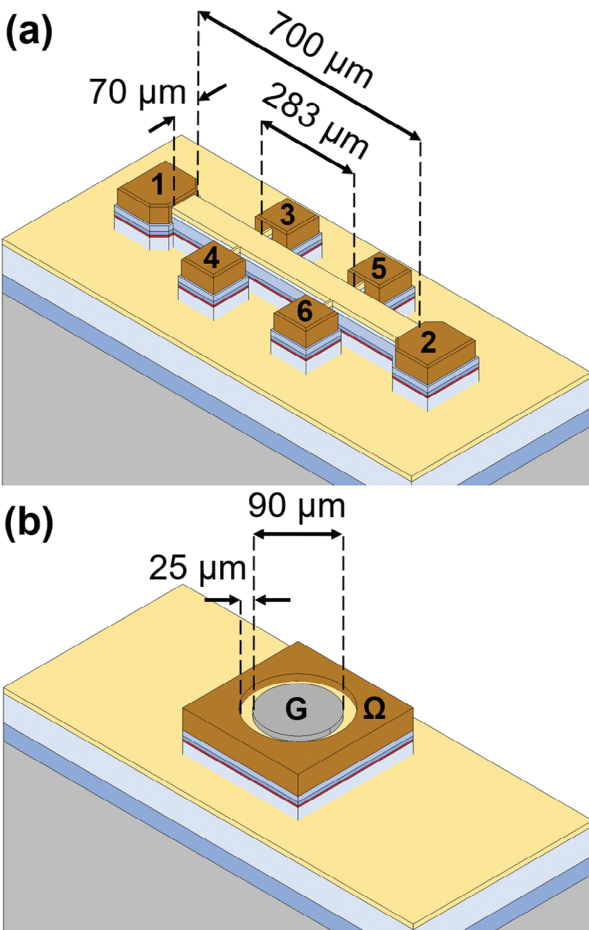


Figure 9. 3D schematic view of a) the Hall bridge and b) the circular device.

6. Experimental Section

Hall effect measurements were performed in Hall bridge configuration with four arms (**Figure 9(a)**). The Hall bridge is 700 μm long, 70 μm wide (W) and the arms are spaced 283 μm apart (D). The current was injected with a Keithley 6220, and the voltage was acquired with a Keithley 2010. Measurements were performed at temperatures ranging from 10 to 600 K. The resistivity is given by the relation $\rho = (W/D)(V_\rho/I)$, where W and D are Hall bridge dimensions, I is the injected current and V_ρ is the measured voltage with no magnetic field applied. The Hall density is given by $n_H = (IB)/(qV_H)$, where q is the electron elementary charge, B is the magnetic field intensity and V_H is the resulting Hall voltage. For the determination of n_H , a magnetic field of $\pm 1 \text{ T}$ was applied, with an injected current of $\pm 40 \mu\text{A}$. Knowing the resistivity and the Hall density, we determine the Hall mobility with the expression $\mu_H = r_H/(q\rho n_H)$. In a degenerated case, where the relaxation time is assumed to be energy-independent (see Section 3), the Hall factor $r_H = \langle \tau^2 \rangle / \langle \tau \rangle^2$ is taken as unity.

Trap detection was carried out using deep level transient spectroscopy (DLTS) with an FT 1230 DLTS system from PhysTech. The characterization was performed on a circular device (**Figure 9(b)**) consisting of a 20/200 nm Ni/Au circular gate contact deposited on top of the SiN layer. The central gate contact (noted G) has a diameter of 90 μm , and is spaced 25 μm apart from the ohmic contact (noted Ω). The sample was placed on a thermal stage within a cryostat. The device was reverse biased with a voltage V_R applied to the gate contact. A pulse voltage V_p was used to fill the traps with a duration of t_p . At the end of the pulse, trapped electrons were thermally emitted. Capacitance transients generated by the thermally emitted

electrons were recorded over a temperature range from 77 to 325 K at a frequency of 1 MHz between times t_0 and $t_0 + T_w$, where t_0 is the cut-off time (or delay) and T_w is the measurement period width. Current-voltage and capacitance-voltage measurements were also conducted on the circular device placed inside the cryostat, and using the PhysTech system.

Electrical simulations of the heterostructure band diagrams were realized in one dimension with a Schrödinger-Poisson solver, using the Nextnano software. The band diagrams were simulated with a gate metal on top of the cap layer, with a resulting barrier height fixed at 0.84 eV, corresponding to the Ni/GaN contact.^[69–71]

Supporting Information

Supporting Information is available from the Wiley Online Library or from the author.

Acknowledgements

This work was supported by the French RENATECH network, and the ANR-11-LABX-0014 within the national network GaNex as well as part of project ACTION (ANR-22-CE05-0028). Thanks to T. H. Ngo for the AFM measurements.

Conflict of Interest

The authors declare no conflict of interest.

Data Availability Statement

The data that support the findings of this study are available in the supplementary material of this article.

Keywords

AlGaN channel high electron mobility transistor, electron mobility, silicon substrate, temperature operation, ultrawide bandgap

Received: February 1, 2024

Revised: March 29, 2024

Published online:

- [1] M. A. Khan, A. Bhattacharai, J. N. Kuznia, D. T. Olson, *Appl. Phys. Lett.* **1993**, *63*, 1214.
- [2] J. He, W. Cheng, Q. Wang, K. Cheng, H. Yu, Y. Chai, *Adv. Electron. Mater.* **2021**, *7*, 2001045.
- [3] M. A. Khan, X. Hu, A. Tarakji, G. Simin, J. Yang, R. Gaska, M. S. Shur, *Appl. Phys. Lett.* **2000**, *77*, 1339.
- [4] V. Kumar, A. Kuliev, T. Tanaka, Y. Otoki, I. Adesida, *Electron. Lett.* **2003**, *39*, 1758.
- [5] C.-H. Lee, W.-R. Lin, Y.-H. Lee, J.-J. Huang, *IEEE Trans. Electron Devices* **2018**, *65*, 488.
- [6] X. Li, M. Van Hove, M. Zhao, K. Geens, W. Guo, S. You, S. Stoffels, V.-P. Lempinen, J. Sormunen, G. Groeseneken, S. Decoutere, *IEEE Electron Device Lett.* **2018**, *39*, 999.
- [7] W. Saito, Y. Takada, M. Kuraguchi, K. Tsuda, I. Omura, *IEEE Trans. Electron Devices* **2006**, *53*, 356.
- [8] S. Karmalkar, U. K. Mishra, *IEEE Trans. Electron Devices* **2001**, *48*, 1515.

- [9] W. Saito, Y. Takada, M. Kuraguchi, K. Tsuda, I. Omura, T. Ogura, H. Ohashi, *IEEE Trans. Electron Devices* **2003**, *50*, 2528.
- [10] H. Xing, Y. Dora, A. Chini, S. Heikman, S. Keller, U. K. Mishra, *IEEE Electron Device Lett.* **2004**, *25*, 161.
- [11] K.-L. Lin, E.-Y. Chang, Y.-L. Hsiao, W.-C. Huang, T. Li, D. Tweet, J.-S. Maa, S.-T. Hsu, C.-T. Lee, *Appl. Phys. Lett.* **2007**, *91*, 222111.
- [12] E. Arslan, M. K. Ozturk, A. Teke, S. Ozcelik, E. Ozbay, *J. Phys. D: Appl. Phys.* **2008**, *41*, 155317.
- [13] K. Cheng, M. Leys, S. Degroote, B. Van Daele, S. Boeykens, J. Derluyn, M. Germain, G. Van Tendeloo, J. Engelen, G. Borghs, *J. Electron. Mater.* **2006**, *35*, 592.
- [14] T. Sugahara, J.-S. Lee, K. Ohtsuka, *Jpn. J. Appl. Phys.* **2004**, *43*, L1595.
- [15] H. Yu, T. Duan, *Gallium Nitride Power Devices*, Jenny Stanford Publishing, New York **2017**, <https://doi.org/10.1201/9781315196626>.
- [16] P. Ferrandis, M. El-Khatib, M.-A. Jaud, E. Morvan, M. Charles, G. Guillot, G. Bremond, *J. Appl. Phys.* **2019**, *125*, 035702.
- [17] P. Ferrandis, M. Charles, Y. Baines, J. Buckley, G. Garnier, C. Gillot, G. Reimbold, *Jpn. J. Appl. Phys.* **2017**, *56*, 04CG01.
- [18] P. Ferrandis, M. Charles, M. Veillerot, C. Gillot, *J. Phys. D: Appl. Phys.* **2020**, *53*, 185105.
- [19] P. Ferrandis, M. Charles, C. Gillot, R. Escoffier, E. Morvan, A. Torres, G. Reimbold, *Microelectron. Eng.* **2017**, *178*, 158.
- [20] P. Ferrandis, M. El-Khatib, M.-A. Jaud, E. Morvan, M. Charles, G. Guillot, G. Bremond, *Semicond. Sci. Technol.* **2019**, *34*, 045011.
- [21] T. Nanjo, M. Takeuchi, M. Suita, Y. Abe, T. Oishi, Y. Tokuda, Y. Aoyagi, *Appl. Phys. Express* **2008**, *1*, 011101.
- [22] T. Nanjo, M. Takeuchi, M. Suita, T. Oishi, Y. Abe, Y. Tokuda, Y. Aoyagi, *Appl. Phys. Lett.* **2008**, *92*, 263502.
- [23] H. Tokuda, M. Hatano, N. Yafune, S. Hashimoto, K. Akita, Y. Yamamoto, M. Kuzuhara, *Appl. Phys. Express* **2010**, *3*, 121003.
- [24] T. Nanjo, A. Imai, Y. Suzuki, Y. Abe, T. Oishi, M. Suita, E. Yagyu, Y. Tokuda, *IEEE Trans. Electron Devices* **2013**, *60*, 1046.
- [25] X. Li, W. Zhang, M. Fu, J. Zhang, H. Jiang, Z. Guo, Y. Zou, R. Jiang, Z. Shi, Y. Hao, *IEICE Electron. Express* **2015**, *12*, 20150694.
- [26] W. Zhang, J. Zhang, M. Xiao, L. Zhang, Y. Hao, *IEEE J. Electron Devices Soc.* **2018**, *6*, 931.
- [27] I. Abid, J. Mehta, Y. Cordier, J. Derluyn, S. Degroote, H. Miyake, F. Medjdoub, *Electronics* **2021**, *10*, 635.
- [28] M. Hatano, N. Kunishio, H. Chikaoka, J. Yamazaki, Z. B. Makhzani, N. Yafune, K. Sakuno, S. Hashimoto, K. Akita, Y. Yamamoto, M. Kuzuhara, *CS MANTECH Conference* **2010**, 101.
- [29] M. Asif Khan, J. W. Yang, W. Knap, E. Frayssinet, X. Hu, G. Simin, P. Prystawko, M. Leszczynski, I. Grzegory, S. Porowski, R. Gaska, M. S. Shur, B. Beaumont, M. Teisseire, G. Neu, *Appl. Phys. Lett.* **2000**, *76*, 3807.
- [30] T. Nanjo, M. Suita, T. Oishi, Y. Abe, E. Yagyu, K. Yoshiara, Y. Tokuda, *Electron. Lett.* **2009**, *45*, 424.
- [31] T. Nanjo, M. Takeuchi, A. Imai, M. Suita, T. Oishi, Y. Abe, E. Yagyu, T. Kurata, Y. Tokuda, Y. Aoyagi, *Electron. Lett.* **2009**, *45*, 1346.
- [32] S. Hashimoto, K. Akita, T. Tanabe, H. Nakahata, K. Takeda, H. Amano, *Phys. Status Solidi* **2010**, *7*, 1938.
- [33] X.-D. Li, J.-C. Zhang, Y. Zou, X.-Z. Ma, C. Liu, W.-H. Zhang, H.-J. Wen, Y. Hao, *Chinese Phys. Lett.* **2015**, *32*, 077205.
- [34] S. Bajaj, F. Akyol, S. Krishnamoorthy, Y. Zhang, S. Rajan, *Appl. Phys. Lett.* **2016**, *109*, 133508.
- [35] A. G. Baca, B. A. Klein, A. A. Allerman, A. M. Armstrong, E. A. Douglas, C. A. Stephenson, T. R. Fortune, R. J. Kaplar, *ECS J. Solid State Sci. Technol.* **2017**, *6*, Q161.
- [36] S. Muhtadi, S. M. Hwang, A. Coleman, F. Asif, G. Simin, M. Chandrashekhar, A. Khan, *IEEE Electron Device Lett.* **2017**, *38*, 914.
- [37] L. Zhang, J.-F. Zhang, W.-H. Zhang, T. Zhang, L. Xu, J.-C. Zhang, Y. Hao, *Chinese Phys. Lett.* **2017**, *34*, 128501.
- [38] A. G. Baca, B. A. Klein, J. R. Wendt, S. M. Lepkowski, C. D. Nordquist, A. M. Armstrong, A. A. Allerman, E. A. Douglas, R. J. Kaplar, *IEEE Electron Device Lett.* **2019**, *40*, 17.
- [39] E. A. Douglas, B. Klein, A. A. Allerman, A. G. Baca, T. Fortune, A. M. Armstrong, *Journal of Vacuum Science & Technology B* **2019**, *37*, 021208.
- [40] J. S. Lundh, B. Chatterjee, Y. Song, A. G. Baca, R. J. Kaplar, T. E. Beechem, A. A. Allerman, A. M. Armstrong, B. A. Klein, A. Bansal, D. Talreja, A. Pogrebnyakov, E. Heller, V. Gopalan, J. M. Redwing, B. M. Foley, S. Choi, *Appl. Phys. Lett.* **2019**, *115*, 153503.
- [41] S. Mollah, M. Gaevski, K. Hussain, A. Mamun, R. Floyd, X. Hu, M. V. S. Chandrashekhar, G. Simin, A. Khan, *Appl. Phys. Express* **2019**, *12*, 074001.
- [42] T. Razzak, S. Hwang, A. Coleman, H. Xue, S. H. Sohel, S. Bajaj, Y. Zhang, W. Lu, A. Khan, S. Rajan, *Appl. Phys. Lett.* **2019**, *115*, 043502.
- [43] Y. Wu, J. Zhang, S. Zhao, W. Zhang, Y. Zhang, X. Duan, J. Chen, Y. Hao, *IEEE Electron Device Lett.* **2019**, *40*, 1724.
- [44] H. Xue, C. H. Lee, K. Hussain, T. Razzak, M. Abdullah, Z. Xia, S. H. Sohel, A. Khan, S. Rajan, W. Lu, *Appl. Phys. Express* **2019**, *12*, 066502.
- [45] M. Hatano, N. Yafune, H. Tokuda, Y. Yamamoto, S. Hashimoto, K. Akita, M. Kuzuhara, *IEICE Trans. Electron.* **2012**, *E95*, 1332.
- [46] N. Yafune, S. Hashimoto, K. Akita, Y. Yamamoto, H. Tokuda, M. Kuzuhara, *Electron. Lett.* **2014**, *50*, 211.
- [47] J. Singh, R. Chaudhuri, A. Hickman, V. Protasenko, H. G. Xing, D. Jena, *APL Mater.* **2022**, *10*, 111120.
- [48] A. Raman, S. Dasgupta, S. Rajan, J. S. Speck, U. K. Mishra, *Jpn. J. Appl. Phys.* **2008**, *47*, 3359.
- [49] B. A. Klein, E. A. Douglas, A. M. Armstrong, A. A. Allerman, V. M. Abate, T. R. Fortune, A. G. Baca, *Appl. Phys. Lett.* **2019**, *114*, 112104.
- [50] J. Mehta, I. Abid, J. Bassaler, J. Pernot, P. Ferrandis, M. Nemoz, Y. Cordier, S. Rennesson, S. Tamariz, F. Semond, F. Medjdoub, *e-Prime – Advances in Electrical Engineering, Electronics and Energy* **2023**, *3*, 100114.
- [51] R. S. Smith, *Electrical characterization of GaAs materials and devices* 1989 (Ed.: D. C. Look), Wiley, Chichester **1993**, *5*, 280.
- [52] D. Zanato, S. Gokden, N. Balkan, B. K. Ridley, W. J. Schaff, *Semicond. Sci. Technol.* **2004**, *19*, 427.
- [53] S. Gokden, R. Baran, N. Balkan, S. Mazzucato, *Phys. E* **2004**, *24*, 249.
- [54] M. N. Gurusinghe, S. K. Davidsson, T. G. Andersson, *Phys. Rev. B* **2005**, *72*, 045316.
- [55] M. Miyoshi, T. Egawa, H. Ishikawa, *Solid-State Electron.* **2006**, *50*, 1515.
- [56] J. Zhang, Y. Hao, J. Zhang, J. Ni, *Sci. China Ser. F-Inf. Sci.* **2008**, *51*, 780.
- [57] B. K. Ridley, B. E. Foutz, L. F. Eastman, *Phys. Rev. B* **2000**, *61*, 16862.
- [58] A. G. Baca, A. M. Armstrong, A. A. Allerman, E. A. Douglas, C. A. Sanchez, M. P. King, M. E. Coltrin, T. R. Fortune, R. J. Kaplar, *Appl. Phys. Lett.* **2016**, *109*, 033509.
- [59] D. Y. Protasov, T. V. Malin, A. V. Tikhonov, A. F. Tsatsulnikov, K. S. Zhuravlev, *Semiconductors* **2013**, *47*, 33.
- [60] M. Miyoshi, S. Fujita, T. Egawa, *Appl. Phys. Express* **2015**, *8*, 051003.
- [61] S. Bajaj, T.-H. Hung, F. Akyol, D. Nath, S. Rajan, *Appl. Phys. Lett.* **2014**, *105*, 263503.
- [62] M. E. Coltrin, A. G. Baca, R. J. Kaplar, *ECS J. Solid State Sci. Technol.* **2017**, *6*, S3114.
- [63] J. L. Hudgins, G. S. Simin, E. Santi, M. A. Khan, *IEEE Trans. Power Electron.* **2003**, *18*, 907.
- [64] C. Consejo, S. Contreras, L. Konczewicz, P. Lorenzini, Y. Cordier, C. Skierbiszewski, J. L. Robert, *Phys. Stat. Sol.* **2005**, *2*, 1438.

- [65] P. Ferrandis, M. Billaud, J. Duvernay, M. Martin, A. Arnoult, H. Grampeix, M. Cassé, H. Boutry, T. Baron, M. Vinet, G. Reimbold, *J. Appl. Phys.* **2018**, *123*, 161534.
- [66] R. Zeisel, M. W. Bayerl, S. T. B. Goennenwein, R. Dimitrov, O. Ambacher, M. S. Brandt, M. Stutzmann, *Phys. Rev. B* **2000**, *61*, R16283.
- [67] M. D. McCluskey, N. M. Johnson, C. G. Van de Walle, D. P. Bour, M. Kneissl, W. Walukiewicz, *Phys. Rev. Lett.* **1998**, *80*, 4008.
- [68] B. A. Klein, A. A. Allerman, A. G. Baca, C. D. Nordquist, A. M. Armstrong, M. Van Heukelom, A. Rice, V. Patel, M. Rosprim, L. Caravello, R. DeBerry, J. R. Pipkin, V. M. Abate, R. J. Kaplar, *J. Microelectron. Electron. Packag.* **2023**, *20*, 1.
- [69] O. Ambacher, J. Smart, J. R. Shealy, N. G. Weimann, K. Chu, M. Murphy, W. J. Schaff, L. F. Eastman, R. Dimitrov, L. Wittmer, M. Stutzmann, W. Rieger, J. Hilsenbeck, *J. Appl. Phys.* **1999**, *85*, 3222.
- [70] L. S. Yu, D. J. Qiao, Q. J. Xing, S. S. Lau, K. S. Boutros, J. M. Redwing, *Appl. Phys. Lett.* **1998**, *73*, 238.
- [71] J. Bassaler, R. Comyn, C. Bougerol, Y. Cordier, F. Medjdoub, P. Ferrandis, *J. Appl. Phys.* **2022**, *131*, 124501.